ACS OMEGA

Open Access

http://pubs.acs.org/journal/acsodf

Article

Unfolding the Photophysical Behavior of Luminescent Polymeric Films Containing β-Diketonate Tetrakis Eu^{III} Complexes via Multilayer Quantum Mechanics

Published as part of ACS Omega special issue "Chemistry in Brazil: Advancing through Open Science".

Leonardo F. Saraiva,[○] Ariane C. F. Beltrame,[○] Airton G. Bispo-Jr,* Felipe S. M. Canisares, Albano N. Carneiro Neto, Renaldo T. Moura Jr,* E. Kraka, Sergio A. M. Lima, and Ana M. Pires*

Cite This: *ACS Omega* 2025, 10, 30563−30575

Read Online

ACCESS | Metrics & More | Article Recommendations | Supporting Information

ABSTRACT: The elucidation of the mechanisms governing the photophysical properties of trivalent lanthanide (Ln^{III}) complexes embedded in polymeric matrices, such as poly(methyl) methacrylate (PMMA) and polyvinylidene fluoride (PVDF), is challenging due to their intricate composite nature. Although theoretical modeling offers insights into film luminescence, conventional computational strategies face significant limitations. Given the large-scale nature of these systems, which encompass thousands of atoms, full-scale quantum mechanical (QM) simulations are impractical. Existing methodologies often integrate molecular mechanics (MM) with QM, yet such hybrid frameworks introduce inaccuracies in excited-state calculations. To address these challenges, this study proposes a multilevel computational protocol employing a hybrid QM/QM approach. Density functional theory (DFT) was used for the $[Eu(dbm)_4]^-$ complex (dbm = 1,3-diphenyl-1,3-propanedione), while the polymeric environment was treated using the GFNn-xTB method. The protocol demonstrated strong agreement between experimental and theoretical emission quantum yields (QY) for both the isolated complex and $[Eu(dbm)_4]^-$/PMMA or PVDF films. Our findings revealed that angular and length distortions in the Eu−O bonds within PVDF were induced by increased packing around the complex, impacting the ligand-Eu^{III} energy transfer by elevating the triplet state energy. These results underscore the predictive capabilities of the hybrid QM/QM strategy, offering a robust alternative for deciphering opto-structural relationships in Ln^{III}-based polymeric films.

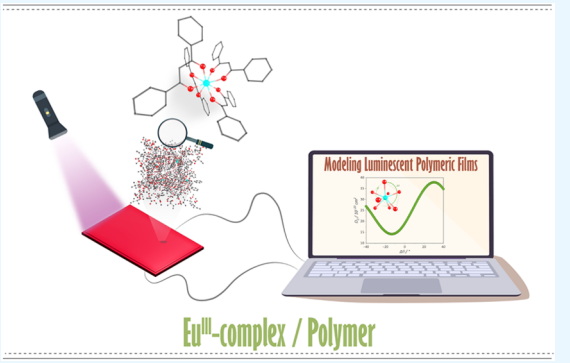

INTRODUCTION

A powerful technique in materials science is to manipulate the structure and composition of materials to control their physical properties.[1] This strategy is widely employed among chemists to optimize material properties for practical market applications. A prominent example is the enhancement of the optical response of molecular cluster-aggregates under ultraviolet (UV) excitation through composition control.[2,3] This methodology can be easily extended to other systems, particularly those based on trivalent lanthanide ions (Ln^{III}), which have been extensively studied due to their intriguing photophysical features. These characteristics include, but are not limited to, sharp emission bands spanning from the near-UV (NUV) to the near-infrared (NIR) spectral regions, high emission quantum yield (QY), and high emission color purity resulting from intraconfigurational $4f \leftrightarrow 4f$ transitions.[4,5] Due to the forbidden nature of these transitions in free ions, direct sensitization of Ln^{III} is inefficient. Consequently, emission-enhancing techniques, such as the coordination of Ln^{III} with organic chromophores are essential,[6] as the ligand can act as an antenna, absorbing energy and transferring it to the Ln^{III} ion.

Among the wide range of organic chromophores, β-diketone ligands have emerged as desirable luminescent antennas,[7] producing bright compounds with notable QYs because of their suitable energy levels for sensitizing Ln^{III}.[8] In this context, tetrakis complexes have been extensively studied in literature,[9,10] as the introduction of a fourth ligand in the coordination sphere can enhance the emission QY by replacing coordinated water molecules and increasing the structural rigidity.[11] Despite significant advances in the development of these complexes, a gap remains in transitioning from molecular

Received: March 15, 2025
Revised: July 1, 2025
Accepted: July 7, 2025
Published: July 12, 2025

https://doi.org/10.1021/acsomega.5c02434
ACS Omega 2025, 10, 30563−30575

designs to materials and ultimately to practical devices, primarily due to their low thermal and photostability.[12,13] To address this challenge, a viable approach lies in dispersing the Ln^{III} complex into polymeric matrices to form luminescent films, thereby improving mechanical, thermal, and optical properties. This strategy entails more attractive materials for potential applications in light-emitting diodes (LEDs),[14] organic-LEDs (OLEDs),[15] luminescent solar concentrators (LSCs),[16] and anticounterfeiting measures.[17,18] Various polymeric matrices have been explored for this purpose, e.g., poly(methyl) methacrylate (PMMA) and polyvinylidene fluoride (PVDF), due to their desirable mechanical and spectroscopic properties.[19−21]

Dispersing Ln^{III} complexes into polymeric matrices often leads to several changes in the photophysical characteristics of the emitter.[12,20,22] These alterations may arise from complex-polymer interactions, which typically lead to structural distortions, modifying the rates of energy transfer (ET) from the antenna to the 4*f* center and directly affecting its sensitization. At first glance, classical spectroscopic techniques can provide valuable initial insights into the photophysical properties of luminescent films; however, they fall short in elucidating mechanisms and features at the atomic and subatomic scales.[23] In such cases, theoretical and computational tools have emerged as viable solutions, offering detailed information and deeper understanding.[24,25] This information is harnessed by modeling the Ln^{III}-based complex, which requires a robust level of theory that accounts for relativistic effects to accurately describe the intricate nature of the 4*f* center.[26,27] When a complex is embedded in a polymeric matrix, the entire system may consist of hundreds to thousands of atoms, making full-scale relativistic simulation infeasible.[28] Therefore, only the coordination compound can be treated at this level of theory.

From this perspective, the treatment of large systems often relies on classical force-fields (FFs) such as *CHARMM*[29,30] or *Amber*.[31] The primary advantage of FFs is their ability to replace costly and complicated electronic structures with classical energy expressions driven by chemical knowledge. However, the required modeling parameters are available for only a limited number of elements,[32] which may restrict their applicability in interdisciplinary research. In recent years, self-parametrized semiempirical quantum mechanical (SP-SQM) methods, such as the tight-binding GFNn-xTB approach,[33] have addressed the shortcomings of standard FFs while improving the accuracy of conventional SQM approaches.[33,34] This advancement has significantly contributed to the field of computational materials by enabling the combination of SP-SQM protocols with higher-level methods, such as density functional theory (DFT). This integration spawns multilevel simulations (QM/QM), allowing large systems,[35] such as luminescent films, to be modeled by treating the complex with DFT and the polymer with GFNn-xTB.[35]

In contrast to these simulations, modeling the photophysical properties of Ln^{III} follows a well-established framework based on Judd−Ofelt theory[36,37] and the ligand-to-Ln^{III} intramolecular energy transfer (IET).[4,38−40] Although these frameworks have been extensively applied to phosphors,[41] glasses,[42] and various coordination compounds,[43] their adaptation to the photophysical properties of complex-polymer films is absent in the literature. This lack of information raises questions about the effects at the atomic and subatomic levels induced by dispersing the complex in the polymer, as well as the perturbation of the excited-state dynamics of these compounds. Therefore, providing models and conducting in-depth analyses of the luminescence-governing dynamics in Ln^{III}-based polymeric films can advance our understanding of their photophysical properties.

Motivated by the pursuit of advancing such understanding, we take on this challenge by introducing a theoretical investigation into the photophysical properties of $[Eu(dbm)_4]$-Q/PMMA and $[Eu(dbm)_4]$Q/PVDF luminescent films (dbm = 1,3-diphenyl-1,3-propanedione, Q = didodecyltimethylammonium, $C_{26}H_{56}N^+$). The $[Eu(dbm)_4]$Q complex was chosen due to its well-elucidated properties, which were previously reported by our research group in a comprehensive experimental study.[44] Regarding polymers, PMMA and PVDF exhibit distinct crystallinity,[45] introducing an intriguing factor for the investigation. By varying the concentration of the complex (0.25−2 wt %) dispersed in the polymer,[14] the photophysical properties changed significantly, underscoring the importance of studying both systems. Beyond elucidating these aspects, we established a correlation between the emission QY and structural distortions induced by switching the polymer from PMMA to PVDF. The outcomes obtained reinforce the feasibility of our proposed protocol, and investigating these mechanisms further has the potential to contribute to the development of Eu^{III}-complex/polymer films with enhanced photophysical features.

METHODOLOGY

Isolated Complex. The initial geometry optimization was performed using a tight grid in the Orca 5.0.3 package[46] at the DFT level, employing the r^{2}SCAN-3c functional. This functional is known for its highly accurate description of large structures[47] and intrinsically incorporates the D4 dispersion correction.[48] All atoms were described by the all-electron Def2-TZVP basis set,[49] except for Eu^{III}, which was treated with "large-core" MWB52 effective core potential (ECP) alongside its corresponding valence basis set.[50,51] After optimization, the minimum energy structure was subjected to a frequency calculation using the numerical Hessian method in the same software with the ωB97x-D4 functional[52] due to its similarity to r^{2}SCAN-3c while offering enhanced accuracy in excited-state energies calculations. This step was necessary to ensure the absence of imaginary frequencies.

Complex/Polymer Film. A miniature chain comprising six monomer units of PMMA and PVDF in the absence of the complex was generated using Packmol software.[53] The miniature chains of both polymers underwent geometry optimization using the r^{2}SCAN-3c functional with the Def2-TZVP basis set.[48,49] Subsequently, the complex/polymer film was constructed by spawning 200 interconnected-miniature chains around the complex. This system was then subjected to geometry optimization based on a self-parametrized force-field calculation using the GFNn-ff method. Starting from the minimum energy configuration of the system, multilevel QM/QM time-dependent DFT (TD-DFT) calculations were performed. In this calculation, the complex was treated using the ωB97x-D4/MWB52/Def2-TZVP method, whereas the polymer was treated with GFN2-xTB. The main aim of this calculation was to extract the energies of the S_1 and T_1 states along with the necessary parameters to determine the IET rates of the complex under polymer influence. It should be highlighted that the counterion was not considered in the calculation, as it could lead to complications due to the large number of atoms that should be treated at high levels.

https://doi.org/10.1021/acsomega.5c02434
ACS Omega 2025, 10, 30563−30575

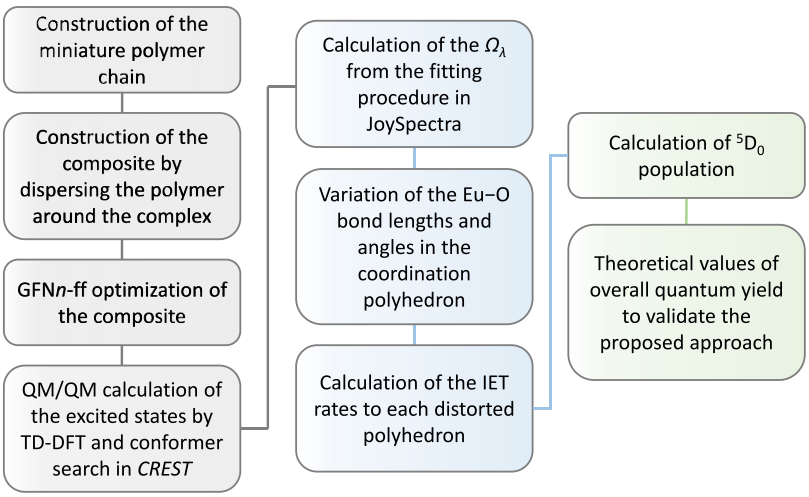

Figure 1. Flowchart for calculating the photophysical parameters for $[Eu(dbm)_4]^-$ in PMMA or PVDF films. The colors in the boxes refer to each step; gray = structural simulations, excited states, and vibrational frequency calculations; blue = determination of Judd–Ofelt intensity parameters (Ω_λ) and IET varying the distortion in the coordination polyhedron; green = computation of the population of the emitter level and theoretical overall emission quantum yield for each film.

Concurrently, a conformer search was conducted using CREST software[54] to obtain optimized conformers with energies similar to those of relaxed complexes. The overall procedure is depicted in Figure 1.

Theoretical Intensity Parameters. The theoretical Judd–Ofelt intensity parameters play a crucial role in providing insights into the chemical environment surrounding Eu^{III}.[55] These parameters include the charge factor (g_j) and the effective polarizability (α'). The former was calculated as outlined in reference[56] using local mode force constants determined from our local vibrational theory,[57] while the latter was obtained through a fitting procedure detailed elsewhere.[58] The experimental parameters varied with concentration; therefore, we adjusted the angles and lengths of the Eu–O bonds in the Eu^{III} coordination polyhedron in *JOYSpectra*[59] to match the experimental values. These experimental values were obtained from a previous study.[14] The geometries resulting from these distortions were then used for intramolecular energy transfer modeling. The equations employed in this step are summarized in the Supporting note S2.

It should be emphasized that, for this step, photophysical calculations were performed only on the optimized structure, as the simulation of intensity parameters depends solely on the coordination polyhedron. Consequently, a systematic evaluation of the photophysical properties for each possible conformer identified in the previous step was deemed unnecessary.

Intramolecular Energy Transfer. The rates of intramolecular energy transfer (IET) from the antenna ligand to Eu^{III} were computed by considering three mechanisms: dipole–dipole (W_{d-d}), dipole–multipole (W_{d-m}), and exchange mechanism (W_{ex}). These calculations were performed according to eqs S8–S16.[60] In all equations, R_L represents the donor–acceptor distance, which was determined using TD-DFT calculations. This parameter is crucial for estimating the rates because W_{d-d} depends on the sixth power on R_L, W_{m-d} depends on the $\lambda+2$ on R_L, and W_{ex} on the fourth power of the donor–acceptor distance. The IET rates were calculated using the equivalent geometry of each distortion, which is necessary to harness the experimental values of the Judd–Ofelt parameters.

Rate Equations and Overall QY. After computing the IET rates, a system of coupled ordinary differential equations (ODEs) was formulated and solved numerically using time propagation to determine the populations of each step in the IET. The set of ODEs was solved using the Radau method, which has been successfully employed in previous studies and has provided reliable results at a feasible computational cost.[61] Thus, each level can be described by a general formula (eq 1):

$$\frac{dP_i(t)}{dt} = \sum_{j=1} W_{j\to i}P_j(t) - \sum_{j=1} W_{i\to j}P_i(t),\ i \neq j \tag{1}$$

where $P_i(t)$ and $P_j(t)$ represent the populations of the i- and j-level at time t, respectively. $W_{j\to i}$ denotes the rate of energy transfer from level j to level i, while $W_{i\to j}$ is the corresponding backward pathway (from i to j).

Each simulation was conducted over a time interval ranging from 0–10 ms with a fixed step-size of 1 μs. By harvesting the population of the emitting level of Eu^{III} ($^5D_0$) and the ground state (S_0) after excitation, the theoretical overall quantum yield can be obtained from eq 2:

$$\Phi_L^{Eu} = \frac{\text{number of photons emitted}}{\text{number of photons absorbed}} = \frac{A_{rad}P_E}{\phi P_0} \tag{2}$$

where A_{rad} is the spontaneous emission coefficient calculated from the Judd–Ofelt intensity parameters,[62] P_E represents the population of the emissive state, P_0 the population of the initial state after excitation, and ϕ denotes the pumping rate. ϕ is directly determined by the expression $\phi = \sigma\rho\lambda_{exc}/hc$,[63] where σ is the absorption cross-section (value of $\sim 10^{-16}$ cm^2 molecule^{-1}), λ_{exc} is the excitation wavelength, h is the constant of Planck, c is the speed of light, and ρ is the power density, which is assumed to be 1 W cm^{-2} in our simulations.

RESULTS AND DISCUSSION

Investigation of Film Structure. The electronic structure of an Ln^{III} coordination compound is intrinsically connected to its symmetry;[64] therefore, accurate geometries are essential when modeling its photophysical properties. This dependence implies that even slight distortions in the ligand scaffold or the

https://doi.org/10.1021/acsomega.5c02434
ACS Omega 2025, 10, 30563–30575

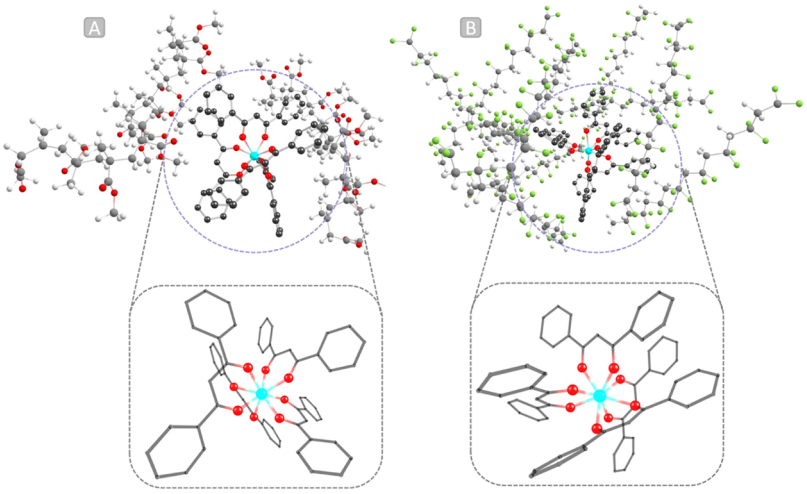

Figure 2. Ground-state QM/QM optimizations of $[Eu(dbm)_4]^-$ in (a) PMMA and (b) PVDF, taken from Figure S3. The complex was treated at the high-level (DFT) and the polymer at the low-level (GFN2-xTB). Hydrogen atoms were hidden for clarity. The color code is as follows: cyan = europium, gray = carbon, green = fluorine, and red = oxygen.

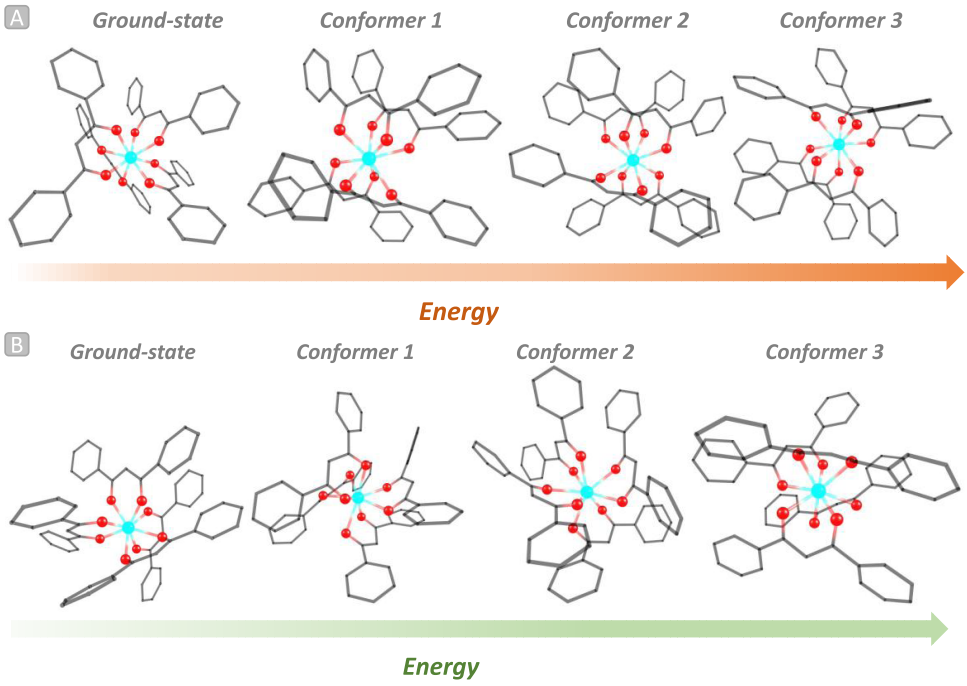

Figure 3. Optimized ground-state at the QM/QM level and their respective conformers in (a) PMMA and (b) PVDF using *CREST* software

Eu^{III} microsymmetry can lead to fluctuations in the photophysical features of Eu^{III}-based complexes.[55] Accordingly, the complex dispersed in PMMA and PVDF was immobilized in the ground state, revealing that the structures belong to a C_1 point group (Figure 2a,b) in both environments. A noticeable degree of distortion was observed between the optimized structures compared with the complex without the polymer. This distortion was qualitatively assessed using the root-mean-square deviation (RMSD), with a value of 0.17 for PMMA and 0.26 for PVDF. One contributing factor to this distortion is the shortening of Eu−O bond (Table S2) in the PVDF environment compared with PMMA, which can be attributed to the packing between the polymer moieties. As evidenced by the polymer structure (Figure S1), PMMA monomers are bulkier than PVDF because of the ester groups attached to the quaternary carbon, resulting in a more spaced distribution around the complex compared to PVDF (Figures S2−S3). Within this framework, since $[Eu(dbm)_4]^-$/PVDF exhibits denser packing than $[Eu(dbm)_4]^-$/PMMA, shorter Eu−O bonds are observed for the complex in the PVDF environment (Figure S4).

Another important aspect to consider is the electronegativity of the constituent atoms of the polymer moieties. As the polymer and the complex come in closer proximity, the oxygen atoms in PMMA or the fluorine atoms in PVDF can interact with hydrogen from the ligand scaffold of the complex, leading to tighter packing.[65] This aligns with the expected electronegativity trend, as F···H interactions are stronger than O···H due to fluorine's higher electronegativity. However, relying solely on packing may not fully address the observed

https://doi.org/10.1021/acsomega.5c02434
ACS Omega 2025, 10, 30563−30575

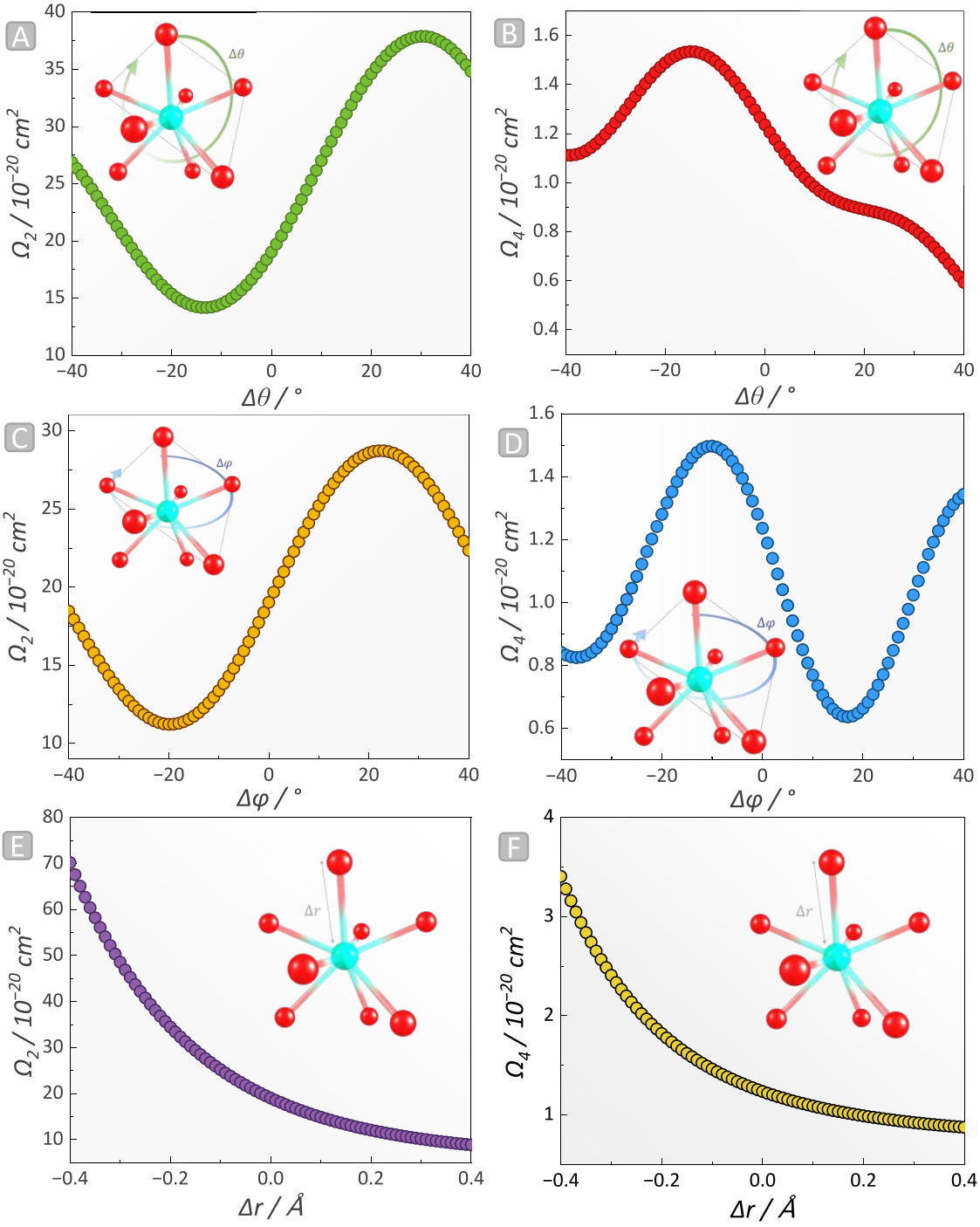

Figure 4. Trends in the theoretical Judd−Ofelt intensity parameters in $[Eu(dbm)_4]^-$/PMMA by varying the θ angle in (a) Ω_2 and (b) Ω_4, φ angle in (c) Ω_2 and (d) Ω_4, followed by variations in the Eu−O distances in (e) Ω_2 and (f) Ω_4.

photophysical features described in the next section. Another perspective was obtained by comparing the $[Eu(dbm)_4]^-$ structure in PMMA and PVDF with the isolated complex. Geometry optimization revealed that the aromatic ring of the isolated complex can rotate out-of-plane (Figure S3). However, when embedded in PMMA, this rotation is practically restricted by short- and long-range interactions between the complex and the polymer's organic groups, allowing only minor rotations due to the available space within the packing. Despite this effect, the restriction was even more pronounced in PVDF, which possesses a semicrystalline[45] and less bulky structure.[66]

It is noteworthy that the computational model employed presupposes an isotropic dispersion of complex particles throughout the polymer matrix. Elemental maps acquired by energy-dispersive X-ray spectroscopy (EDS, Figures S5−S8) demonstrate Eu^{III} agglomerates dispersed throughout the polymer − a typical behavior of complex/polymer films.[67−69] Yet, PVDF comprises coexisting amorphous and crystalline phases, and given the resolution limits of the equipment, it is not possible to guarantee equivalent interactions with both

https://doi.org/10.1021/acsomega.5c02434
ACS Omega 2025, 10, 30563−30575

structural regimes.[70] Consequently, the simulation treats the complex as residing in an amorphous environment, omitting periodic boundary conditions. Incorporating these conditions would have increased the computational cost, which is beyond the scope of the proposed protocol. Furthermore, a full structural characterization of these films was provided in our earlier work.[14]

A wealth of information can be obtained from the analysis of the optimized geometries (Figure 2), particularly concerning the coordination polyhedron in Figure S4, which exhibits a distorted square antiprismatic geometry due to the 8-fold coordination. However, the interpretation of these findings requires caution because variations in symmetry can be implicated depending on the influence of the polymer during film production. An exploration of the conformers revealed the existence of three additional analogous structures in the presence of PMMA and PVDF (Figure 3) with energies similar to those of the optimized system at the QM/QM level. Among these geometries, conformers number three in PMMA and number two in PVDF exhibit C_s symmetry in the coordination polyhedra. Although these groups represent low-symmetry point groups, this alteration confirms that structural distortions are often influenced by packing effects. Moreover, this outcome suggests that multiple conformations may be present in the film. However, this aspect is beyond the scope of this work because it introduces complexities that cannot be addressed using the software and approximations employed.

Theoretical Judd−Ofelt Analysis. With an atomic-level representation of the molecular distortion in both environments of the complex, it becomes feasible to delve into the subatomic scale of these compounds, particularly their electronic structure. The emission bands assigned to intraconfigurational $4f\leftrightarrow4f$ transitions are explained by the Judd−Ofelt theory, whose centerpiece lies in three intensity parameters ($\Omega_{2,4,6}$), from which the transition probabilities, radiative lifetime, and other photophysical features can be directly obtained.[71,72] For Eu^{III}-based compounds, these parameters are directly associated with the emission bands assigned to $^5D_0\rightarrow{}^7F_{2,4,6}$ electronic transitions, and they vary according to their rates, using the magnetic dipole allowed $^5D_0\rightarrow{}^7F_1$ transition as reference.[26] However, Ω_λ (λ = 2, 4, 6) are often interpreted beyond their phenomenological nature, being directly correlated with chemical trends, such as distortions, ligand polarizability, rigidity, covalency, among others.[73]

From this perspective, Ω_2 is widely used throughout papers to describe the degree of distortion in Eu^{III} microssymmetry in terms of Eu−L angular variations,[55,74] while Ω_4 is said to reflect changes in the Eu−L bond covalency.[41,55] Although these qualitative aspects have been discussed for Eu^{III}-based complexes,[55] it is important to question whether quantitative trends align with qualitative ones. The answer to this question lies in Figure 4, where we varied the spherical coordinates (r,θ,φ) of a certain plane of atoms in the Eu^{III} coordination polyhedron (Figures S9−S10). It is worth emphasizing that any influence of alternative conformers can be effectively accounted for by adjusting the coordinates of the ligand atoms within the coordination polyhedron. The behavior of the Ω_6 parameter with these distortions will not be studied because the $^5D_0\rightarrow{}^7F_6$ emission was not observed due to the limitations of the apparatus.[14]

The variation of Ω_2 in terms of θ and φ followed a sinusoidal form by varying 1.5° to an adaptive step in the − 40 to 40° range, where the absolute values derived from Figure 4 are presented in Tables S3−S8. This change can be correlated with those promoted by altering the concentration of the complex in PMMA, which modified the experimental parameters due to the chemical environment around $[Eu(dbm)_4]^-$. By considering the angles θ and φ, the plane of oxygen is distorted in the − 11 to 12° range, where a negative degree indicates a deformation in the counterclockwise direction. An interesting outcome of this analysis is that not every angular deformation augments the value of Ω_2, as the sinusoidal shape tends to decrease after its peak in the 20−25° region in the clockwise direction. These observations stem from the induction of a more symmetric environment at higher angle distortions, which becomes less symmetric when the sinusoidal shape is repeated. This hypothesis is experimentally interpreted as the variation in the emission band associated with $^5D_0\rightarrow{}^7F_2$ transition, simultaneous to the induced distortion.

Concomitantly with θ and φ, varying the Eu−O bond lengths yielded the trend shown in Figure 4e, where an exponential dependence of Ω_2 with Δr was noticed. This behavior is driven by the hypersensitive character of $^5D_0\rightarrow{}^7F_2$ transition, explained by the dynamic coupling (DC) mechanism,[75] which lies in the polarizability of the chemical environment surrounding the Ln^{III}.[76] In this context, Ω_2 reflects both the angular distortion and polarizability of Eu^{III} microssymetry. However, the dominant effect remains elusive since both phenomena occur simultaneously. Thus, using Ω_2 to probe properties such as covalency may not always yield the correct outcome.

Regarding the Ω_4 parameter, it becomes evident from Figure 4b the nondefined shape of the variations in the values by distorting the θ angles, peaking in the counterclockwise 20° region. In contrast, changing φ yielded a well-defined sinusoidal pattern with a maximum value of 1.52×10^{-20} cm^2. The lower dependence of Ω_4 on the angular distortions is noteworthy in this analysis. To understand this behavior, the phenomena can be analyzed from both physical and chemical perspectives. From a physical standpoint, when the Eu^{III} coordination polyhedron becomes more symmetrical, the odd-crystal field quantities, particularly Γ_p^t (representing the DC mechanism), with lower ranks tend to approach zero more rapidly than those with higher ranks, as they are more dependent on the spherical coordinates.[55,76] In this context, lower-rank quantities are more sensitive to angular distortions, meaning that Ω_2 is more responsive to θ and φ than Ω_4 and, subsequently, Ω_6. From a chemical perspective, the nearly symmetry-independent character of $^5D_0\rightarrow{}^7F_4$ transition results in Ω_4 only slightly affected by angular deformations.[23,74] Analogous to the exponential trend of Ω_2 with fluctuations in bond length, a similar pattern is observed for Ω_4 (Figure 4f), where this parameter is highly sensitive to these displacements. In this case, it is worth noting that the negative values of Δr express lengths shorter than the equilibrium bond length. Another important aspect that can be derived is that the participation of bond overlap polarizability (Table S9), a measure of the covalency degree,[77] is higher for Ω_4 (Table S10), suggesting that Ω_4 is more suited to investigate the covalency trends for this complex.

The same analysis can be extended to the $[Eu(dbm)]^-$/PVDF film, where the trends in the Judd−Ofelt intensity parameters are highlighted in Figure S11. All variations followed a pattern similar to that of the PMMA film, except for the changes in $\Omega_{2,4}$ when varying θ. The values of Ω_2 are

https://doi.org/10.1021/acsomega.5c02434
ACS Omega 2025, 10, 30563−30575

higher for PVDF than for PMMA due to larger distortions and the induction of a more polarizable environment, which was observed due to the greater packing, as previously discussed. As the PVDF molecules approach the complex, the complex undergoes distortions that amplifies its polarizability. Therefore, a combination of these two factors enhances the Ω_2 by 2-fold compared with the isolated complex. To achieve the correct theoretical values, distortion occurred in the plane of oxygen in the equatorial region instead of the axial region because the oxygen in the out-of-plane region of Figures S9−S10 forms an almost symmetrical plane. Thus, when this Eu−O bond is deformed, this possibility is restricted, leading to higher Ω_2. From a chemical perspective, we can associate these values with the rates of $^5D_0 \rightarrow {}^7F_2$ transition, because in the Wybourne formalism, a higher number of odd terms (28) are found for C_1 symmetry than for C_s (16 terms),[78,79] elevating the intensity of the band.

Despite the variations in Ω_2, the most pronounced difference between PMMA and PVDF films in terms of Judd−Ofelt analysis lies in the 6-fold increase of Ω_4 (Tables S11−S16). An interesting outcome provided by Figure S11 is that no angular variation (θ,φ) resulted in the experimental values of Ω_4, implying that deformations in Eu^{III} microssymetry play a minor role in these values. However, when varying the Eu−O bond lengths, the theoretical values approached the experimental ones, decreasing the lengths to an extent of 0.5 Å, which is higher than all displacements observed for the PMMA film.

As previously demonstrated, parameter Ω_4 is better suited to evaluate covalency trends because of the higher contribution of bond overlap polarizability (α_{OP}). In this sense, Figure S12 displays the overlap integral and the α_{OP} in terms of absolute variation in bond length ($R' = R_{eq} + \Delta r$, where R_{eq} represents the equilibrium length, Δr the variations in Figures 3 and 4, and R' the absolute variation). Because the equilibrium bond length was taken as 2.529 Å, the variations reported in Table S16 were responsible for the experimental values of Ω_4, leading R' to nearly 2 Å, resulting in a 2.5-fold increase in the polarizability of the bond (Figure S12) and therefore the covalency degree. Hence, it is reasonable to suggest that in the PVDF film, the polymer molecules, along with their packing, induce a more distorted and covalent environment than PMMA, directly influencing other photophysical properties, such as the quantum yield of the film.

Energy Transfer and Quantum Yield. The theoretical Judd−Ofelt intensity parameters enabled the exploration of various photophysical features of the complex within both polymeric environments. Among these properties, energy transfer (ET) assumes paramount importance because of its direct correlation with the emission QY.[62] To determine ET rates, calculations were conducted via TD-DFT at the QM/QM level for both polymers to extract singlet and triplet energy positions alongside donor−acceptor distances. The values acquired are summarized in Tables S17−S19, accompanied by a graphical representation of the state composition in terms of molecular orbital (MO) contributions in Figures S13 and S14, which correspond to the complex in PMMA and PVDF, respectively.

A meticulous inspection of the isosurfaces of these MOs revealed an antibonding character concentrated within the high-electron-density region, i.e., the resonant region of the ligand scaffold. Notably, as these isosurface shift toward the aromatic rings, an increase in the donor−acceptor distance (R_L) becomes apparent. R_L, defined as the distance between the centroid position of the MOs weighted by their coefficients (donor) and Eu^{III} (acceptor), demonstrates that even small changes significantly affect intramolecular energy transfer (IET) rates.[60,61] This sensitivity arises because of the dependence on the sixth power of the dipole−dipole and the fourth power of the ET exchange mechanism, as detailed in eqs S8−S10.

The rates of energy transfer and back-energy transfer (BET), derived by employing the values reported in Table S19, indicate the suitability of the ligand set for sensitizing the Eu^{III} ion, as the ET rate outperforms the BET (Tables S20−S21). This mitigates an additional deactivation pathway that could quench Eu^{III} emission. Intriguingly, although the R_L value of the complex in PVDF is lower, the ET of the T_1 state (W_T) for $[Eu(dbm)_4]^-$/PMMA exceeds $[Eu(dbm)_4]^-$/PVDF by an order of magnitude. This discrepancy arises from the lower energy of the T_1 state of $[Eu(dbm)_4]^-$/PMMA by 1000 cm^{-1}, overshadowing the 0.02 Å difference in R_L. Consequently, this difference leads to nearly a 2-fold increase in BET rates for $[Eu(dbm)_4]^-$/PVDF compared to $[Eu(dbm)_4]^-$/PMMA, quenching the luminescence by deactivating Eu^{III} excited levels.[80] The increase in the BET is associated with reducing the energy gap in the primary BET pathway, i.e., $T_1 \leftarrow ({}^7F_1 \rightarrow {}^5G_2)$, which displays values of − 4229 and − 3230 cm^{-1} for the complex in PMMA and PVDF, respectively (Tables S20 − S21). Regarding ET stemming from the S_1 level, a parallel trend is observed, where, for $[Eu(dbm)_4]^-$/PMMA, the ET rates exceed those of $[Eu(dbm)_4]^-$/PVDF due to the lower R_L values for S_1 (Table S19). Therefore, Tables S20−S21 underscore that ET via the exchange mechanism predominates for the T_1 state, where $^5D_1$ is the main acceptor (considering the $^7F_0 \rightarrow {}^5D_1$ pathway). Such a result means that $^5D_0$ is mostly populated due to the relaxation of the $^5D_1$ manifold. Concurrently, ET from the S_1 state is primarily constituted by dipole and multipole interactions. However, high ET rates are obtained for the $S_1 \rightarrow ({}^7F_1 \rightarrow {}^5G_2)$ pathway, where the exchange mechanism emerges as the leading one. This phenomenon is rooted in ET selection rules for 2^λ-pole, which entail $|J - J'| \leq \lambda \leq J + J'$, and for exchange, $|J - J'| = 0$, 1, thereby inhibiting the dipole and multipole contribution for the $^7F_1 \rightarrow {}^5G_2$ pathway.[4,81]

Distorting the Eu^{III} coordination polyhedron varies the values of $\Omega_{2,4}$ as shown in the previous section, thereby altering the ET and BET rates. Given that the primary pathway of ET stems from the T_1 state, our focus centers on this level to assess the IET rates by manipulating the spherical coordinates (r,θ,φ), as shown in Figure S15. Within this framework, we observe a nonlinear relationship between ET and coordinate variation for the complex in PMMA and PVDF. Despite this trend, the 2% film exhibited the highest ET value, implying that the sensitization of Eu^{III} reaches its peak at this concentration. Concurrently, the BET rates followed a similar pattern, with an exception observed in the case of 2 wt % $[Eu(dbm)_4]^-$ in PVDF, where BET reached its lowest value. Interestingly, for PVDF, the rates of ET and BET remained the same until 1 wt % varying θ and φ angles, with the absolute values highlighted in Tables S22−S25. This outcome aligns with expectations given that $\Omega_{2,4}$ underwent identical variations in both scenarios.

To understand the origin of the photophysical characteristics of the films, exploring beyond ET rates becomes pivotal, considering other potential deactivation routes. To address this issue, a diagram depicting the ligand-to-Eu^{III} energy transfer

https://doi.org/10.1021/acsomega.5c02434
ACS Omega 2025, 10, 30563−30575

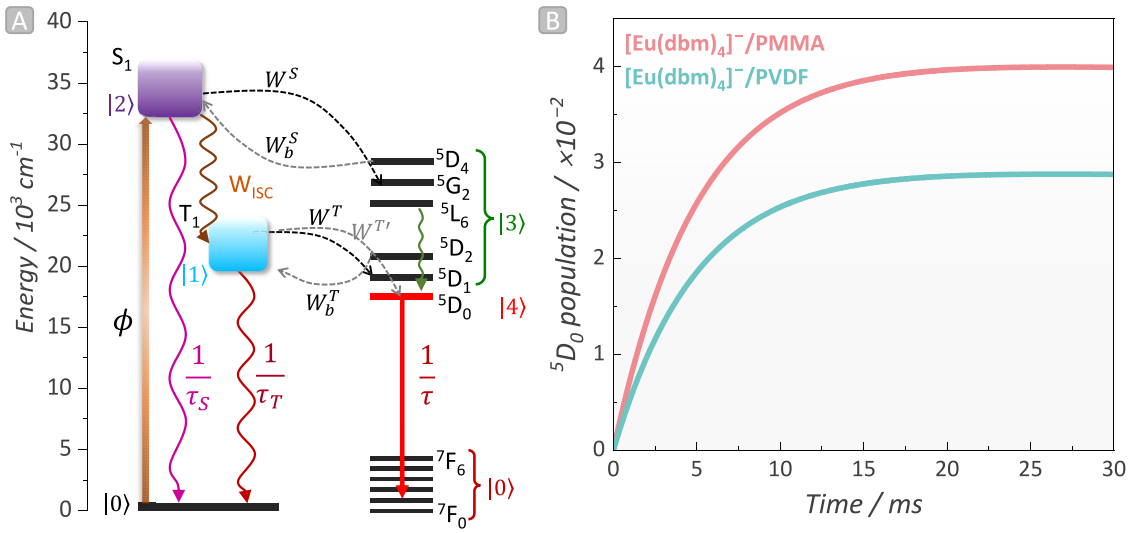

Figure 5. (a) Representative partial energy level diagram of the complex showing the ligand-centered singlet (S) and triplet (T) state energies as well as $^{2S+1}L_J$ levels of Eu^{III}. The ligand absorption (light orange arrow), intersystem crossing (ISC, intense orange), ligand-to-Eu^{III} energy transfer (ET, black and gray dashed arrows), back-ET (light gray dashed arrows), relaxation (green wavy arrow), and Eu^{III} emission (red arrow) processes are also represented. (b) Population kinetics of Eu^{III} $^5D_0$ excited state of the complex for the 0.50 wt % film.

pathways along with plausible deactivation mechanisms was proposed (Figure 5a). The above analysis led to the formulation of a set of coupled ODEs based on eq 1 outlined in the methodology, enabling the capture of population kinetics (eq 3). Within this set of ODEs, various states, such as the ground state (S_0 at $t = 0$, transitioning to ^7F_J at $t \neq 0$), T_1, and S_1 are defined as $|0\rangle$, $|1\rangle$ and $|2\rangle$, respectively. $|3\rangle$ represents any Eu^{III} manifold other than $^5D_0$, while $|4\rangle$ is the $^5D_0$ level. The lifetime decay values of S_1, T_1, and $^5D_0$ states, assigned as τ_S, τ_T, and τ, respectively, assume values in the range of 1 ns−1 μs for τ_S, 1 μs−1 ms for τ_T, and 1 ms for τ.[82] The intersystem crossing (ISC) rates denoted as W_{ISC} were estimated to be around 10^8 s^{-1}, considering the energy gaps between S_1 and T_1 within 10,000 to 15,000 cm^{-1},[61] consistent with the studied complex (12457 cm^{-1} for $[Eu(dbm)_4]^-$/PMMA and 11421 cm^{-1} for $[Eu(dbm)_4]^-$/PVDF). The deactivation pathway: $^5D_1 \rightarrow {}^5D_0$ ($W_{3\rightarrow4}$) ranges from 10^4–10^5 s^{-1}, as presented in a previous study.[83] It is worth noting that the population dynamics are heavily reliant on the chosen boundary conditions,[84] ensuring that the total population across all energy levels remains constant at any given time t within the employed interval. The main outcome of this simulation is depicted in Figure 5b, highlighting a notably higher population of the $^5D_0$ state for $[Eu(dbm)_4]^-$/PMMA compared to $[Eu(dbm)_4]^-$/PVDF, which aligns with the higher experimental quantum yield of the film reported in reference.[14]

$$|0\rangle: \frac{d}{dt}P_0 = -\phi P_0 + \frac{1}{\tau_T}P_1 + \frac{1}{\tau_S}P_2 + \frac{1}{\tau}P_4 \tag{3a}$$

$$|1\rangle: \frac{d}{dt}P_1 = -\left(\frac{1}{\tau_T} + W^T + W^{T'}\right)P_1 + W_{ISC}P_2 + W_b^T P_3 \tag{3b}$$

$$|2\rangle: \frac{d}{dt}P_2 = -\left(\frac{1}{\tau_S} + W^S + W_{ISC}\right)P_2 + W_b^S P_3 + \phi P_0 \tag{3c}$$

$$|3\rangle: \frac{d}{dt}P_3 = -(W_b^S + W_b^T + W_{3\rightarrow4})P_3 + W^T P_1 + W^S P_2 \tag{3d}$$

$$|4\rangle: \frac{d}{dt}P_4 = -\left(\frac{1}{\tau}\right)P_4 + W^{T'}P_1 + W_{3\rightarrow4}P_3 \tag{3e}$$

From Figure S16,S17, notably, for PMMA, the most significant change in population with increasing complex concentration occurred by varying θ. The 2 wt % concentration demonstrated the highest population (0.0415) compared with the 0.25 wt % (0.0373), which is consistent with the highest experimental emission lifetime observed for this film, as indicated in reference.[14] When varying φ and r, minimal population fluctuations were observed (Figure S17a), consistent with the energy transfer trends shown in Figure S15, where the rates reached their peak with θ (1.170×10^8 s^{-1} for the T_1). In contrast, PVDF exhibited nearly constant population behavior as a function of concentration, owing to the small alterations in ET rates with increasing doping amount. Consequently, population variations hovered around the 4×10^{-4} range (Figure S17b). This phenomenon underscores that the population alone may not be fully entitled to elucidate the emission quantum yield of films because the theoretical quantum yield values also rely on the radiative decay of $^5D_0$, as outlined in the methodology.

Given the population values in the dynamic regime (Table S26), the pumping rate, and the theoretical radiative decay estimated from eqs S20–S22, we derive the theoretical values of quantum yield (Φ_L^{Eu}) summarized in Table 1, along with the aforementioned photophysical properties. Notably, in down-shifting systems such as the ones under study, Φ_L^{Eu} remains independent of the excitation power density.[16] This observation stems from the fact that when the pumping rate is increased n-fold, the ratio between the population of the emitting level and the ground state is also enhanced by n-fold.[85] This is due to the proportional augmentation of the emitting-level population alongside the depletion of the ground-state.

https://doi.org/10.1021/acsomega.5c02434
ACS Omega 2025, 10, 30563−30575

Table 1. Experimental and Theoretical Photophysical Parameters: Radiative Decay (A_{rad}) and Overall Quantum Yield (Φ_L^{Eu}) of the Isolated Complex, PMMA, and PVDF Films[a]

wt %	A_{rad}^{exp}/s^{-1}	A_{rad}^{theo}/s^{-1}	exp. Φ_L^{Eu}/%	theo. Φ_L^{Eu}/%
		$[Eu(dbm)_4]^-$		
	652	663	6.40	6.98
		$[Eu(dbm)_4]^-$/PMMA		
0.25	574	579	0.20	0.29
0.50	521	530	0.40	0.52
0.75	764	772	2.20	2.43
1.00	815	821	22.0	24.1
2.00	835	844	40.0	45.2
		$[Eu(dbm)_4]^-$/PVDF		
0.50	944	951	2.70	2.95
0.75	970	979	14.0	16.2
1.00	879	886	5.80	6.21
2.00	1011	1025	21.0	23.3

[a]The pumping rate used to estimate the overall quantum yield was 198.9 s^{-1} under 395 nm excitation. All experimental values were adapted from the Supporting Information (Table S2) of reference 14, with permission from the Royal Society of Chemistry.

The reported values in Table 1 display a well-desired agreement between the theoretical and experimental values of the radiative decays and emission quantum yields. Interestingly, dispersing the complex within the polymer matrix led to a minimum 3-fold increase in the quantum yield at the highest complex concentration. This enhancement is associated with amplified distortions in Eu^{III} microssymmetry, since the trends in Ω_2 indicate that as the concentration increases, angular deformations in the coordination polyhedron intensify. This potentially relaxes the constraints imposed by the selection rules for the $^5D_0 \rightarrow {}^7F_2$ transition. This hypothesis is supported by experimental and theoretical trends in radiative decay rates. Another factor that needs to be considered is the escalated ET values from the triplet state with increasing concentration, which play a crucial role in the $^5D_0$ population and influence the quantum yield.

From an experimental perspective, the $^5D_0$ level is susceptible to deactivation by high-energy oscillations like O−H and O−O oscillators in water and air, respectively.[12,14,86] Consequently, the polymer might play a protective role by avoiding a reduction in the radiative decay rate, thereby enhancing the emission quantum yield due to higher values of A_{rad}. In contrast to $[Eu(dbm)_4]^-$/PMMA, no clear trend was observed in the emission quantum yield for $[Eu(dbm)_4]^-$/PVDF. Intriguingly, the 1 wt % PVDF sample exhibited a higher value of Φ_L^{Eu} than the 0.50 wt % sample, despite having lower radiative decay (Table 1). However, in comparison to the 0.75 wt % sample, an anomalous trend is observed, since the latter presents a higher Φ_L^{Eu}. This counterintuitive occurrence can be explained by two main hypotheses: (*i*) faster ET due to the shortening of Eu−O bond induced by the PVDF. (*ii*) Faster depletion of the excited-state (Figures S16−S17), which reduces P_0 that presents an inversely proportional relationship with the quantum yield (eq 2), resulting in higher values of Φ_L^{Eu} compared to the 0.5 wt %, and lower than the 0.75 wt %.

These findings imply that higher QYs are achieved not only by optimizing the IET but also by increasing the population and radiative decay of the $^5D_0$ manifold. Hence, to strategize luminescent films with enhanced performance, one should move beyond IET alone by also considering influences such as the structural properties of the complex embedded in polymers. This effect may indirectly influence population dynamics. For example, the simulations evinced a more compact arrangement of PVDF molecules around the complex, which induced a higher triplet state energy for the $[Eu(dbm)_4]^-$/PVDF system compared to $[Eu(dbm)_4]^-$/PMMA, thereby affecting the sensitization mechanism. Hence, manipulating the organic groups in the polymer surrounding Eu^{III} is crucial for the design of systems. Although the modeling protocol for the PVDF film targets the amorphous fraction, the sizable distortions needed to reproduce the experimental values unequivocally underscore the influence of the semicrystalline domains − an essential factor for shedding light on the material luminescence dynamics. Such occurrences are an illustrative example of how the proposed protocol can lead the way to understanding and predicting the capabilities of luminescent films. The notable alignment between the experimental and theoretical quantum yield values while maintaining a low computational cost endorses the suitability of the proposed protocol. In this sense, integrating QM/QM calculations with the modeling of Ln^{III} photophysical characteristics proves to be a valuable strategy for designing films with enhanced luminescence.

CONCLUSIONS

In this study, an in-depth investigation of $[Eu(dbm)_4]^-$ dispersed in PMMA and PVDF matrices was conducted using multilevel quantum mechanical methods to model the photophysical properties of Ln^{III}-based compounds. An interesting outcome of the simulation was that the tighter packing of PVDF around the complex resulted in pronounced distortion of the ligand scaffold and Eu^{III} microssymmetry. These angular changes were the primary cause of the elevated Ω_2 values, whereas substantial alterations in polarizability led to a 6-fold increase in Ω_4. This increase can be attributed to the modifications of the coordination polyhedron of Eu^{III}, which reduced Eu−O bond lengths. Considering these distortions in terms of spherical coordinates allowed us to estimate the energy transfer and back-energy transfer rates. A higher concentration of the complex in the composition boosted the ET and BET rates by an uneven factor. Intriguingly, the $[Eu(dbm)_4]^-$/PVDF film displayed lower ET rates by an order of magnitude compared to $[Eu(dbm)_4]^-$/PMMA, which reflected in the lower population of the $^5D_0$ level for PVDF and consequently, reduced QY. This outcome underscores the predictive capability of our proposed methodology while shedding light on the mechanisms controlling the photophysical attributes of complex/polymer systems. These findings pave the way for materials development by strategically selecting systems where distortion occurs. Further studies aimed at detailing complex-polymer interactions via the composition of normal modes of these complexes are expected to offer deeper insights into the influence of the polymer on the photophysical attributes of these composites.

ASSOCIATED CONTENT

Supporting Information

The Supporting Information is available free of charge at https://pubs.acs.org/doi/10.1021/acsomega.5c02434.

https://doi.org/10.1021/acsomega.5c02434
ACS Omega 2025, 10, 30563−30575

Further details of the theoretical methodology employed in this study, including the models and equations. The supporting materials also include experimental SEM and EDS analysis of the film. The outcomes harnessed by the system of ordinary differential equations to harvest the population of the emissive state are also shown (PDF)

AUTHOR INFORMATION

Corresponding Authors

Airton G. Bispo-Jr − *Institute of Chemistry, University of São Paulo (USP), 05508-900 São Paulo, Brazil*; Email: airton.bispo.junior@iq.usp.br

Renaldo T. Moura Jr − *Academic Unit of Cabo de Santo Agostinho, Federal Rural University of Pernambuco (UFRPE), 54518-430 Cabo de Santo Agostinho, Brazil*; Email: renaldotmjr@gmail.com

Ana M. Pires − *Department of Chemistry and Biochemistry, School of Science and Technology, São Paulo State University (UNESP), 19060-900 Presidente Prudente, Brazil; Institute of Biosciences, Humanities and Exact Sciences, Department of Chemistry and Environmental Sciences, São Paulo State University (UNESP), 15054-000 São José do Rio Preto, Brazil*; orcid.org/0000-0001-9607-0510; Phone: +55 16 997835059; Email: ana.maria@unesp.br

Authors

Leonardo F. Saraiva − *Department of Chemistry and Biochemistry, School of Science and Technology, São Paulo State University (UNESP), 19060-900 Presidente Prudente, Brazil; Institute of Biosciences, Humanities and Exact Sciences, Department of Chemistry and Environmental Sciences, São Paulo State University (UNESP), 15054-000 São José do Rio Preto, Brazil; Department of Physics, University of Aveiro, 3810-193 Aveiro, Portugal*; orcid.org/0000-0002-1963-9854

Ariane C. F. Beltrame − *Department of Chemistry and Biochemistry, School of Science and Technology, São Paulo State University (UNESP), 19060-900 Presidente Prudente, Brazil; Institute of Biosciences, Humanities and Exact Sciences, Department of Chemistry and Environmental Sciences, São Paulo State University (UNESP), 15054-000 São José do Rio Preto, Brazil; Department of Sustainable Development and Ecological Transition (DISSTE), University of Eastern Piedmont "A. Avogadro", 13100 Vercelli, Italy*

Felipe S. M. Canisares − *Institute of Chemistry, University of São Paulo (USP), 05508-900 São Paulo, Brazil*

Albano N. Carneiro Neto − *Department of Physics, University of Aveiro, 3810-193 Aveiro, Portugal*; orcid.org/0000-0003-2432-0992

E. Kraka − *Department of Chemistry (Computational and Theoretical Chemistry Group), Southern Methodist University (SMU), 75725 Dallas, Texas, United States*; orcid.org/0000-0002-9658-5626

Sergio A. M. Lima − *Department of Chemistry and Biochemistry, School of Science and Technology, São Paulo State University (UNESP), 19060-900 Presidente Prudente, Brazil; Institute of Biosciences, Humanities and Exact Sciences, Department of Chemistry and Environmental Sciences, São Paulo State University (UNESP), 15054-000 São José do Rio Preto, Brazil*

Complete contact information is available at: https://pubs.acs.org/10.1021/acsomega.5c02434

Author Contributions

○L.F.S. and A.C.F.B. contributed equally to this study. A.C.F.B. designed the films and cowrote the article. L.F.S. performed all calculations, interpreted data, and cowrote the article. A.G.B.-J. cowrote the article and participated in the film production. F.S.M.C. cowrote the article and participated in the film production. A.N.C.N. cowrote the article and participated in the calculations. R.T.M.Jr cowrote the article and participated in calculations. E.K., S.A.M.L., and A.M.P. codesigned the methodology, cowrote the article, and provided the resources for the research.

Funding

The Article Processing Charge for the publication of this research was funded by the Coordenacao de Aperfeicoamento de Pessoal de Nivel Superior (CAPES), Brazil (ROR identifier: 00x0ma614).

Notes

The authors declare no competing financial interest.

ACKNOWLEDGMENTS

The authors are grateful for the financial support provided by FAPESP (2023/05718-9; 2023/16684-8), CAPES (88887.672234/2022-00), and CNPq (309448/2021-2; 308868/2022-6), the National Science Foundation, NSF, grant CHE 2102461, and the computations supplied by the Center of Scientific Computing (NCC/GridUnesp) no. 137 of São Paulo State University. R.M.T.Jr thanks CNPq, Grant numbers 406483/2023-0, 310988/2023-3, and 404742/2024-6.

ABBREVIATIONS

QY–quantum yield; ET–energy transfer; BET–back-energy transfer; DFT–density functional theory; QM–quantum mechanics; SQM–semiempirical quantum mechanics; SP-SQM–self-parametrized semiempirical quantum mechanics; PMMA–poly(methyl) methacrylate; PVDF–polyvinylidene fluoride; dbm–1,3-diphenyl-1,3-propanedione

REFERENCES

(1) Gálico, D. A.; Kitos, A. A.; Ovens, J. S.; Sigoli, F. A.; Murugesu, M. Lanthanide-Based Molecular Cluster-Aggregates: Optical Barcoding and White-Light Emission with Nanosized {Ln_{20}} Compounds. *Angew. Chem., Int. Ed.* **2021**, *60*, 6130−6136.

(2) Gálico, D. A.; Murugesu, M. Inside-Out/Outside-In Tunability in Nanosized Lanthanide-Based Molecular Cluster-Aggregates: Modulating the Luminescence Thermometry Performance via Composition Control. *ACS Appl. Mater. Interfaces* **2021**, *13* (39), 47052−47060.

(3) Calado, C. M. S.; Gálico, D. A.; Murugesu, M. Composition Control in Molecular Cluster-Aggregates: A Toolbox for Optical Output Tunability *via* Energy Transfer Pathways. *ACS Appl. Mater. Interfaces* **2023**, *15* (37), 44137−44146.

(4) Carneiro Neto, A. N.; Teotonio, E. E. S.; de Sá, G. F.; Brito, H. F.; Legendziewicz, J.; Carlos, L. D.; Felinto, M. C. F. C.; Gawryszewska, P.; Moura, R. T., Jr; Longo, R. L.; Faustino, W. M.; Malta, O. L. Chapter 310-Modeling intramolecular energy transfer in lanthanide chelates. A critical review and recent advances. *Handb. Phys. Chem. Rare Earths* **2019**, *56*, 55−162.

(5) Ferreira da Rosa, P. P.; Kitagawa, Y.; Shoji, S.; Oyama, H.; Imaeda, K.; Nakayama, N.; Fushimi, K.; Uekusa, H.; Ueno, K.; Goto,

H.; Hasegawa, Y. Preparation of photonic molecular trains via soft-crystal polymerization of lanthanide complexes. *Nat. Commun.* **2022**, *13*, No. 3660.
(6) Thor, W.; Wu, Y.; Wang, L.; Zhang, Y.; Tanner, P. A.; Wong, K.-L. Charging and ultralong phosphorescence of lanthanide facilitated organic complex. *Nat. Commun.* **2021**, *12*, No. 6532.
(7) Dalal, A.; Nehra, K.; Hooda, A.; Singh, D.; Kumar, P.; Kumar, S.; Malik, R. S.; Rathi, B. Luminous lanthanide diketonates: Review on synthesis and optoelectronic characterizations. *Inorg. Chim. Acta* **2023**, *550*, No. 121406.
(8) Sato, S.; Wada, M. Relations between Intramolecular Energy Transfer Efficiencies and Triplet State Energies in Rare Earth β-diketone Chelates. *Bull. Chem. Soc. Jpn.* **1970**, *43* (7), 1955−1962.
(9) Costa, I. F.; Blois, L.; Paolini, T. B.; Assunção, I. P.; Teotonio, E. E. S.; Felinto, M. C. F. C.; Moura-Jr, R. T.; Longo, R. L.; Fastino, W. M.; Dias, L. C.; Malta, O. L.; Carneiro Neto, A. N.; Brito, H. F. Luminescence Properties of lanthanide tetrakis complexes as molecular light emitters. *Coord. Chem. Rev.* **2024**, *502*, No. 215590.
(10) Binnemans, K. Chapter 225 - Rare-earth beta-diketonates. *Handb. Phys. Chem. Rare Earths* **2005**, *35*, 107−272.
(11) Pham, Y. H.; Trush, V. A.; Carneiro Neto, A. N.; Korabik, M.; Sokolnick, J.; Weselski, M.; Malta, O. L.; Amirkhanov, V. M.; Gawryszewska, P. Lanthanide complexes with *N*-phosphorylated carboxamide as UV converters with excellent emission quantum yield and single-ion magnet behavior. *J. Mater. Chem. C* **2020**, *8*, 9993−10009.
(12) de Freitas, B. D.; Onish, B. S. D.; Caixeta, F. J.; Bortoletto-Santos, R.; Garcia, F. D. R.; Massadeq, Y.; Ribeiro, S. J. L. Green host urethanesil based on castor oil doped with Eu^{3+} complex. *Opt. Mater.* **2023**, *138*, No. 113706.
(13) Leite Silva, C. M. B.; Bispo-Jr, A. G.; Lima, S. A. M.; Pires, A. M. Eu^{3+} complex/polymer films for light-emitting diode applications. *Opt. Mater.* **2019**, *96*, No. 109323.
(14) Beltrame, A. C. F.; Bispo-Jr, A. G.; Canisares, F. S. M.; Fernandes, R. V.; Laureto, E.; Lima, S. A. M.; Pires, A. M. PMMA or PVDF films blended with β-diketonate tetrakis Eu^{III} or Tb^{III} complexes used as downshifting coatings of near-UV LEDs. *Soft Matter* **2023**, *19*, 3992−4000.
(15) Ilmi, R.; Zhang, D.; Tensi, L.; Al-Sharji, H.; Al Rasbi, N. K.; Macchioni, A.; Zhou, L.; Wong, W. Y.; Raithby, P. R.; Khan, M. S. Salts of Lanthanide(III) Hexafluoroacetylacetonates [Ln = Sm(III), Eu(III) and Tb(III)] with Dipyridylammonium cations: Synthesis, characterization, photophysical properties and OLED fabritcation. *Dyes Pigm.* **2022**, *203*, No. 110300.
(16) Biju, S.; Freire, R. O.; Eom, Y. K.; Scopelliti, R.; Bünzli, J. C. G.; Kim, H. K. A Eu^{III} Tetrakis(β-diketonate) Dimeric Complex: Photophysical Properties, Structural Elucidation by Sparkle/AM1 Calculations, and Doping into PMMA Films and Nanowires. *Inorg. Chem.* **2014**, *53* (16), 8407−8417.
(17) Alam, N.; Mondal, S.; Hossain, S. K. S.; Sahoo, S.; Sarma, D. Lanthanide-Directed Luminescent "Soft" Coordination Polymer Gels: White Light Emission, Anticounterfeiting, and Thin-Film-Based Sensing. *ACS Appl. Eng. Mater.* **2023**, *1* (4), 1201−1212.
(18) Dias, L. M. S.; Fu, L.; Pereira, R. F. P.; Carneiro Neto, A. N.; De Zea Bermudez, V.; André, P. S.; Ferreira, R. A. S. Envolving photonic authentication with sustainable luminescent smart e-tags. *FlexMat* **2024**, *1* (2), 116−126.
(19) Gil-Kowalczyk, M.; Łyszczek, R.; Jusza, A.; Piramidowicz, R. Thermal, Spectroscopy and Luminescent Characterization of Hybrid PMMA/Lanthanide Complex Materials. *Materials* **2021**, *14* (12), 3156.
(20) Francisco, L. H. C.; Felinto, M. C. F. C.; Brito, H. F.; Teotonio, E. E. S.; Malta, O. L. Development of highly luminescent PMMA films doped with Eu^{3+} β-diketonate coordinated on ancillary ligand. *J. Mater. Sci.: Mater. Electron.* **2019**, *30* (18), 16922−16931.
(21) Assunção, I. P.; Blois, L.; Cauli, F. P.; Felinto, M. C. F. C.; Malta, O. L.; Brito, H. F. Luminescence under UV(A, B and C) and sunlight exposure of tetrakis Tb^{3+} carboxylate complexes doped in different polymers. *J. Alloys Compd.* **2024**, *1002*, No. 175319.
(22) Caixeta, F. J.; Saraiva, L. F.; Freitas, B. D.; Onishi, B. S.; Santagneli, S. H.; Bortoletto-Santos, R.; Pires, A. M.; Ribeiro, S. J. L. Spectroscopic and theoretical tools unravel the thermally-stabilized behavior of Eu^{3+}-Based complex incorporated in sustainable urethanesil film. *Chem. - Asian J.* **2025**, *20* (9), No. e202401612.
(23) Saraiva, L. F.; Bispo-Jr, A. G.; Lima, S. A. M.; Pires, A. M. Unrevealing the opto-structural features of luminescente polymeric films containing Eu^{III}-doped phosphors through spectroscopic and theoretical perspectives. *J. Mater. Chem. C* **2023**, *11*, 14226−14236.
(24) McCarver, G. A.; Hinde, R. J.; Vogiatzis, K. D. Selecting Quantum-Chemical Methods for Lanthanide-Containing Molecules: A Balance between Accuracy and Efficiency. *Inorg. Chem.* **2020**, *59* (15), 10492−10500.
(25) Diogenis, I. M. S.; Bispo, A. G., Jr.; Pirovani, R. V.; Saraiva, L. F.; Gozzo, F. C.; Correia, C. R. D.; Mazali, I. O.; Nome, R. A.; Sigoli, F. A. Towards opto-structural parameters to enhance the circularly polarized luminescence brightness of Eu^{III} β-diketone complexes with chiral auxiliary ligands. *J. Mater. Chem. C* **2024**, *12*, 5097−5107.
(26) Saraiva, L. F.; Bispo, A. G., Jr; Lima, S. A. M.; Pires, A. M. Eu^{3+}-activated $SrY_2O_4:Ce^{4+/3+}$ red-phosphor for WLEDs: Structural and luminescence insights from experimental and theoretical perspectives. *J. Alloys Compd.* **2023**, *938*, No. 168595.
(27) Saraiva, L. F.; Carneiro Neto, A. N.; Bispo-Jr, A. G.; Quintano, M. M.; Kraka, E.; Carlos, L. D.; Lima, S. A. M.; Pires, A. M.; Moura, R. T., Jr. Role of Vibronic Coupling for the Dynamics of Intersystem Crossing in Eu^{3+} Complexes: An avenue for Brighter Compounds. *J. Chem. Theory Comput.* **2025**, *21* (6), 3066−3076.
(28) Plett, C.; Grimme, S. Automated and Efficient Generation of General Molecular Aggregate Structures. *Angew. Chem., Int. Ed.* **2023**, *62* (4), No. e202214477.
(29) Momany, F. A.; Rone, R. Validation of the general purpose QUANTA R3.2/CHARMm force field. *J. Comput. Chem.* **1992**, *13* (7), 888−900.
(30) MacKerell, A. D., Jr; Banavali, N.; Foloppe, N. Development and current status of the CHARMM force field for nucleic acids. *Biopolymers* **2000**, *56* (4), 257−265.
(31) Salomon-Ferrer, R.; Case, D. A.; Walker, R. C. An overview of the Amber biomolecular simulation package. *WIREs Comput. Mol. Sci.* **2013**, *3*, 198−210.
(32) Spicher, S.; Grimme, S. Robust Atomistic Modeling of Materials, Organometallic, and Biochemical Systems. *Angew. Chem., Int Ed.* **2020**, *59* (36), 15665−15673.
(33) Bannwarth, C.; Ehlert, S.; Grimme, S. GFN2-xTB−An Accurate and Broadly Parametrized Self-Consistent Tight-Binding Quantum Chemical Method with Multipole Electrostatic and Density-Dependent Dispersion Contributions. *J. Chem. Theory Comput.* **2019**, *15* (3), 1652−1671.
(34) Christensen, A. S.; Kubar, T.; Cui, Q.; Elstner, M. Semiempirical Quantum Mechanical Methods for Noncovalent Interactions for Chemical and Biochemical Applications. *Chem. Rev.* **2016**, *116* (9), 5301−5337.
(35) Plett, C.; Katbashev, A.; Ehlert, S.; Grimme, S.; Bursch, M. ONIOM meets xtb: efficient, accurate, and robust multi-layer simulations across the periodic table. *Phys. Chem. Chem. Phys.* **2023**, *25*, 17860−17868.
(36) Judd, B. R. Optical Absorption Intensities of Rare-Earth Ions. *Phys. Rev.* **1962**, *127*, 750−761.
(37) Ofelt, G. S. Intensities of Crystal Spectra of Rare-Earth Ions. *J. Chem. Phys.* **1962**, *37*, 511−520.
(38) Malta, O. L. Mechanism of non-radiative energy transfer involving lanthanides ions revisited. *J. Non-Cryst. Solids* **2008**, *354*, 4770−4776.
(39) Malta, O. L. Ligand-rare Earth ion energy transfer in coordination compounds: A theoretical approach. *J. Lumin.* **1997**, *71*, 229−236.
(40) e Silva, F. R. G.; Malta, O. L. Calculation of the ligand-lanthanide ion energy transfer rate in coordination compounds: contribution exchange interactions. *J. Alloys Compd.* **1997**, *250* (1−2), 427−430.

https://doi.org/10.1021/acsomega.5c02434
ACS Omega 2025, 10, 30563−30575

(41) Shyichuk, A.; Moura, R. T., Jr; Carneiro Neto, A. N.; Runowski, M.; Zarad, M. S.; Szczeszak, A.; Lis, S.; Malta, O. L. Effects of Dopant Addition on Lattice and Luminescence Intensity Parameters of Eu(III)-Doped Lanthanum Orthovanadate. *J. Phys. Chem. C* **2016**, *120* (50), 28497−28508.
(42) El-Hady, M. M.; Morshidy, H. Y.; Hassan, M. A. Judd-Ofelt analysis, optical and structural features of borate glass doped with erbium oxide. *J. Lumin.* **2023**, *263*, No. 119972.
(43) Bispo-Jr, A. G., Jr.; Saraiva, L. F.; Lima, S. A. M.; Pires, A. M.; Mazali, I. O.; Sigoli, F. A. Lanthanide coordination polymers as luminescent thermometers: integrating theoretical modeling with experimental analysis to tune the thermal response. *J. Mat Chem. C* **2025**, *13*, 3320−3330.
(44) Leite Silva, C. M. B.; Bispo-Jr, A. G.; Canisares, F. S. M.; Castilho, S. A.; Lima, S. A. M.; Pires, A. M. Eu^{3+}-tetrakis β-diketonate complexes for solid-state lighting application. *Luminescence* **2019**, *34* (8), 877−886.
(45) Zhou, Y.; Liu, W.; Tan, B.; Zhu, C.; Ni, Y.; Fang, L.; Lu, C.; Xu, Z. Crystallinity and β Phase Fraction of PVDF in Biaxiality Stretched PVDF/PMMA Films. *Polymers* **2021**, *13* (7), 998.
(46) Neese, F. Software update: The ORCA program system − Version 5.0. *Wires Comp. Mol. Sci.* **2022**, *12*, No. e1606.
(47) Grimme, S.; Hansen, A.; Ehlert, S.; Mewes, J.-M. r^2SCAN-3c: A "Swiss army knife" composite electronic-structure method. *J. Chem. Phys.* **2021**, *154*, No. 064103.
(48) Müller, M.; Hansen, A.; Grimme, S. ωB97X-3c: A composite range-separated hybrid DFT method with a molecule-optimized polarized valence double-ζ basis set. *J. Chem. Phys.* **2023**, *158*, No. 014103.
(49) Weigend, F.; Ahlrichs, R. Balanced basis sets of split valence, triple zeta valence and quadruple zeta valence quality for H to Rn: Design and assessment of accuracy. *Phys. Chem. Chem. Phys.* **2005**, *7*, 3297−3305.
(50) Dolg, M.; Stoll, H.; Savin, A.; Preuss, H. Energy-adjusted pseudopotentials for the rare earth elements. *Theoret. Chim. Acta* **1989**, *75*, 173−194.
(51) Dolg, M.; Stoll, H.; Preuss, H. A combination of quasirelativistic pseudopotential and ligand field calculations for lanthanoid compounds. *Theoret. Chim. Acta* **1993**, *85*, 441−450.
(52) Chai, J.-D.; Head-Gordon, M. Long-range corrected hybrid density functionals with damped atom-atom dispersion corrections. *Phys. Chem. Chem. Phys.* **2008**, *10*, 6615−6620.
(53) Martínez, L.; Andrade, R.; Birgin, E. G.; Martínez, J. M. PACKMOL: A package for Building initial configurations for molecular dynamics simulations. *J. Comput. Chem.* **2009**, *30*, 2157 DOI: 10.1002/jcc.21224.
(54) Grimme, S. Exploration of Chemical Compound, Conformer, and Reaction Space with Meta-Dynamics Simulations Based on Tight-Binding Quantum Chemical Calculations. *J. Chem. Theory Comput.* **2019**, *15* (5), 2847−2862.
(55) Moura, R. T.; Carneiro Neto, A. N.; Longo, R. L.; Malta, O. L. On the calculation and interpretation of covalency in the intensity parameters of 4f-4f transitions in Eu^{3+} complexes based on the chemical bond overlap polarizability. *J. Lumin.* **2016**, *170*, 420−430.
(56) Moura, R. T., Jr; Quintano, M.; Santos, C. V., Jr; Albuquerque, V. A. C. A.; Aguiar, E. C.; Kraka, E.; Carneiro Neto, A. N. Featuring a new computational protocol for the estimation of intensity and overall quantum yield in lanthanide chelates with applications to Eu(III) mercapto-triazole Schiff base ligands. *Opt. Mater.:X* **2022**, *16*, No. 100216.
(57) Kraka, E.; Quintano, M.; La Force, H. W.; Antonio, J. J.; Freindorf, M. The Local VIbrational Mode Theory and Its Place in the Vibrational Spectroscopy Arena. *J. Phys. Chem. A* **2022**, *126* (47), 8781−8798.
(58) Santos-Jr, C. V.; Aguiar, E. C.; Carneiro Neto, A. N.; Moura, R. T., Jr Adaptive guided stochastic optimzation: A novel approach for fitting the theoretical intensity parameters for lanthanide compounds. *Opt. Mater.:X* **2023**, *20*, No. 100275.
(59) Moura, R. T., Jr.; Carneiro Neto, A. N.; Aguiar, E. C.; Santos-Jr, C. V.; de Lima, E. M.; Faustino, W. M.; Teotonio, E. E. S.; Brito, H. F.; Felinto, M. C. F. C.; Ferreira, R. A. S.; Carlos, L. D.; Longo, R. L.; Malta, O. L. JOYSPectra: A web platform for luminescence of lanthanides. *Opt. Mater.:X* **2021**, *11*, No. 100080.
(60) Malta, O. L.; Gonçalves e Silva, F. R. A theoretical approach to intramolecular energy transfer and emission quantum yields in coordination compounds of rare earth ions. *Spectrochim. Acta, Part A* **1998**, *54*, 1593−1599.
(61) Carneiro Neto, A. N.; Mamontova, E.; Botas, A. M. P.; Brites, C. D. S.; Ferreira, R. A. S.; Rouquette, J.; Guari, Y.; Larionova, J.; Long, J.; Carlos, L. D. Rationalizing the Thermal Response of Dual-Center Molecular Thermometers: The Example of na Eu/Tb Coordination Complexes. *Adv. Opt. Mater.* **2022**, *10* (5), No. 2101870.
(62) Bünzli, J.-C. On the design of highly luminescent lanthanide complexes. *Coord. Chem. Rev.* **2015**, *293*−*294*, 19−47.
(63) Fang, M.; Carneiro Neto, A. N.; Fu, L.; Ferreira, R. A. S.; deZeaBermudez, V.; Carlos, L. D. A Hybrid Materials Approach for Fabricating Efficient WLEDs Based on Di-Ureasils Doped with Carbon Dots and a Europium Complex. *Adv. Mater. Technol.* **2022**, *7*, No. 2100727.
(64) Kaappa, S.; Malola, S.; Häkkinen, H. Point Group Analysis of the Electronic Structure of Bare and Protected Metal Nanocrystals. *J. Phys. Chem. A* **2018**, *122* (84), 8576−8584.
(65) Srikanth, A.; Abrams, C. F. Effect of molecular packing and hydrogen bonding on the properties of epoxy-amido amine systems. *Comput. Mater. Sci.* **2019**, *169*, No. 109082.
(66) Wang, S.; Yuan, K.; Wang, K.; Chen, W.; Yamada, K.; Barkley, D.; Koga, T.; Hong, Y.-L.; Miyoshi, T. Intramolecular and intermolecular packing in polymer crystallization. *Macromolecules* **2019**, *52* (12), 4739−4748.
(67) de Souza, J. M.; Alves, S., Jr.; Sá, G. F.; Azevedo, W. M. Doped polymers with Ln(III) complexes: simulation and control of light colors. *J. Alloys Compd.* **2002**, *344* (1−2), 320−322.
(68) Mahmood, Z.; Aleem, A. R.; Sial, Q. A.; Wang, G.; Usman, M.; Khokhar, W. A.; Wei, C.; Liu, X.; Ding, W. Eu^{3+} embedded hybrid fluorescent membrane for Ultrasensitive and efficient sensing of Cu^{2+} in aqueous media. *Dyes Pig.* **2024**, *226*, No. 112106.
(69) Hayashi, J.; Shoji, S.; Kitagawa, Y.; Hasegawa, Y. Amorphous lanthanide complex for organic luminescent materials. *Coord. Chem. Rev.* **2022**, *467*, No. 214607.
(70) Bispo-Jr, A. G.; Oliveira, N. A.; Cardoso, C. X.; Lima, S. A. M.; Job, A. E.; Osorio-Román, I. O.; Danna, C. S.; Pires, A. M. Red-light emitting polymer composite based on PVDF membranes and Europium phosphor using Buriti Oil as plasticizer. *Mater. Chem. Phys.* **2018**, *217*, 160−167.
(71) Ćirić, A.; Marciniak, L.; Dramicanin, M. D. Self-referenced method for the Judd-Ofelt parametrisation of the Eu^{3+} excitation spectrum. *Sci. Rep.* **2022**, *12*, No. 563.
(72) Blois, L.; Carneiro Neto, A. N.; Longo, R. L.; Costa, I. F.; Paolini, T. B.; Brito, H. F.; Malta, O. L. On the experimental Determination of 4*f*-4*f* Intensity Parameters from the Emission Spectra of Europium(III) Compounds. *Opt. Spectrosc.* **2022**, *130*, 10−17.
(73) Hehlen, M. P.; Brik, M. G.; Krämer, K. W. 50th anniversary of the Judd-Ofelt theory: An experimentalist's view of the formalism and its application. *J. Lumin.* **2013**, *136*, 221−239.
(74) Binnemans, K. Interpretation of europium(III) spectra. *Coord. Chem. Rev.* **2015**, *295*, 1−45.
(75) Thor, W.; Carneiro Neto, A. N.; Moura, R. T., Jr.; Wong, K.-L.; Tanner, P. A. Europium(III) coordination chemistry: structure, spectra and hypersensitivity. *Coord. Chem. Rev.* **2024**, *517*, No. 215927.
(76) Malta, O. L.; Carlos, L. D. Intensities of 4f-4f transitions in glass materials. *Quim. Nova* **2003**, *26* (6), 889−895.
(77) Malta, O. L.; Batista, H. J.; Carlos, L. D. Overlap polarizability of a Chemical bond: a scale of covalency and application to lanthanide compounds. *Chem. Phys.* **2002**, *282* (1), 21−30.

https://doi.org/10.1021/acsomega.5c02434
ACS Omega 2025, 10, 30563−30575

(78) Suta, M.; Cimpoesu, F.; Urland, W. The angular overlap model of ligand field theory for f elements: An intuitive approach building bridges between theory and experiment. *Coord. Chem. Rev.* **2021**, *441*, No. 213981, DOI: 10.1016/j.ccr.2021.213981.
(79) Wybourne, B. G.; Meggers, W. F. Spectroscopic Properties of Rare Earths. *Phys. Today* **1965**, *18* (9), 70−72.
(80) Hasegawa, Y.; Kitagawa, Y. Luminescent lanthanides coordination polymers with transformative energy transfer processes for physical and chemical sensing applications. *J. Photochem. Photobiol., C* **2022**, *51*, No. 100485.
(81) Tanner, P. A.; Zhou, L.; Duan, C.; Wong, K.-L. Misconceptions in electronic energy transfer: bridging the gap between chemistry and physics. *Chem. Soc. Rev.* **2018**, *47*, 5234−5265.
(82) Kasprzycka, E.; Carneiro Neto, A. N.; Trush, V. A.; Malta, O. L.; Jerzykiewicz, L.; Amirkhanov, V. M.; Legendziewicz, J.; Gawryszewska, P. Spectroscopic aspects for the Yb^{3+} coordination compound with a large energy gap between the ligand Yb^{3+} excited states. *Spectrochim. Acta, Part A* **2022**, *274*, No. 1210172.
(83) Saraiva, L. F.; Bispo, A. G., Jr.; Costa, A. L.; Sigoli, F. A.; Lima, S. A. M.; Pires, A. M. Dimensionality reduction expands the frontiers of lanthanide luminescence thermometry beyond single-parametric thermal sensing. *Chem. Mater.* **2025**, *37* (9), 3125−3136.
(84) Blois, L.; Carneiro Neto, A. N.; Malta, O. L.; Brito, H. F. The role of the $Eu^{3+7}F_1$ level in the direct sensitization of the $^5D_0$ emitting level through intramolecular energy transfer. *J. Lumin.* **2022**, *247*, No. 118862.
(85) Ramalho, J. F. C. B.; Carneiro Neto, A. N.; Carlos, L. D.; André, P. S.; Ferreira, R. A. S. Lanthanides for the new Generation of optical sensing and internet of things. *Handb. Phys. Chem. Rare Earths* **2022**, *61*, 31−128.
(86) Tanner, P. A.; Thor, W.; Zhang, Y.; Wong, K.-L. Energy Transfer Mechanism and Quantitative Modeling of Rate from an Antenna to a Lanthanide ion. *J. Phys. Chem. A* **2022**, *126* (41), 7418−7431.

https://doi.org/10.1021/acsomega.5c02434
ACS Omega 2025, 10, 30563−30575